



# Integrated microwave acousto-optic frequency shifter on thin-film lithium niobate

LINBO SHAO,<sup>1,5</sup>  NEIL SINCLAIR,<sup>1,2</sup> JAMES LEATHAM,<sup>3</sup> YAOWEN HU,<sup>1</sup> MENGJIE YU,<sup>1</sup>  TERRY TURPIN,<sup>4</sup> DEVON CROWE,<sup>3</sup> AND MARKO LONČAR<sup>1,6</sup>

<sup>1</sup>John A. Paulson School of Engineering and Applied Sciences, Harvard University, 29 Oxford Street, Cambridge, MA 02138, USA

<sup>2</sup>Division of Physics, Mathematics and Astronomy, and Alliance for Quantum Technologies (AQT), California Institute of Technology, 1200 E. California Blvd., Pasadena, CA 91125, USA

<sup>3</sup>Raytheon Space & Airborne Systems, 2000 E. El Segundo Ave., El Segundo, CA 90245, USA

<sup>4</sup>49918 Evergreen Ave., Columbia, MD 21046, USA

<sup>5</sup>shaolb@seas.harvard.edu

<sup>6</sup>loncar@seas.harvard.edu

**Abstract:** Electrically driven acousto-optic devices that provide beam deflection and optical frequency shifting have broad applications from pulse synthesis to heterodyne detection. Commercially available acousto-optic modulators are based on bulk materials and consume Watts of radio frequency power. Here, we demonstrate an integrated 3-GHz acousto-optic frequency shifter on thin-film lithium niobate, featuring a carrier suppression over 30 dB. Further, we demonstrate a gigahertz-spaced optical frequency comb featuring more than 200 lines over a 0.6-THz optical bandwidth by recirculating the light in an active frequency shifting loop. Our integrated acousto-optic platform leads to the development of on-chip optical routing, isolation, and microwave signal processing.

© 2020 Optical Society of America under the terms of the [OSA Open Access Publishing Agreement](#)

## 1. Introduction

Integrated acousto-optic or Brillouin scattering devices [1] have enabled a wide range of applications including frequency shifting [2–5], microwave-to-optical conversion (modulation) [6–11], microwave photonic filtering [12], frequency comb generation [13], pulse shaping [14], ultra-narrow-linewidth lasing [15,16], and nonreciprocal transmission [17–23]. Such integrated devices employ photoelasticity and optical confinement of thin-film materials such as silicon [16,17,19–21], silicon nitride [15], aluminum nitride [4,5,14,22,23], gallium arsenide [6], arsenic trisulfide [12], lithium tantalate [13], and lithium niobate (LN) [7–11]. Acousto-optic frequency shifters (AOFSs) deflect the light into a different spatial mode and shift its optical frequency by the acoustic frequency. Commercial AOFSs [24] employ bulk acoustic waves and provide outstanding extinction ratio, large carrier suppression, and high efficiencies for large optical bandwidths. However, they are large discrete components and require a few Watts of radio frequency (RF) power. For example, a free-space tellurium dioxide acousto-optic modulator (G&H AOMO 3110-197) operates at 110 MHz, consumes 2.0 W RF power, and deflects >90% of the input light around 1060 nm; a fiber-pigtailed AOFS (Brimrose IPF-1500-1550-3FP) operates at 1.5 GHz, deflects 3-10% of the input light to the first order output fiber. To develop integrated AOFSs, surface acoustic waves have been employed to deflect light confined by an ion diffused layer [2], but its relatively large optical mode size (a few microns) limits interactions with sub-micron-wavelength gigahertz acoustic waves. Recently, electromechanically driven suspended acousto-optic waveguides have been utilized to achieve frequency shifts exceeding 10 GHz [4,5] but suffer from low efficiencies of  $\sim 10^{-5}$  and weak carrier suppression. In addition to AOFSs, electro-optic devices can achieve optical frequency shifting by destructive interference

between Mach-Zehnder modulators [25,26], by serrodyne frequency shifting [27–29], and by employing electro-optic cavities [30–32].

Here, we demonstrate integrated gigahertz AOFSs on thin-film LN, which leverage the large piezoelectric and photoelastic coefficients of LN, as well as its low microwave and optical propagation loss. Benefiting from the fact that both optical and acoustic indices (phase velocities) of LN are greater (smaller) than those of the underlying silicon dioxide, we construct fully supported AOFSs, thereby providing improved robustness and a more straightforward fabrication process than suspended acousto-optic devices. Specifically, at the telecommunication wavelength of 1.5  $\mu\text{m}$ , we demonstrate an optical frequency shift of 3 GHz with carrier suppression over 30 dB and the opposite sideband suppression >40 dB (below the noise floor). Furthermore, as an application of our device, we demonstrate a 3-GHz optical frequency comb with more than 200 lines over a 0.6-THz (5 nm) optical bandwidth by recirculating light in the active frequency shifting loop with our AOFS and an erbium-doped fiber amplifier (EDFA).

## 2. Device design and fabrication

Our integrated AOFSs are fabricated using an 800-nm-thick X-cut LN thin film on a 2- $\mu\text{m}$ -thick silicon dioxide layer on a silicon substrate (Fig. 1(a)). The phase matching condition between the light and acoustic wave (Fig. 1(a) inset) determines the optimum incident (Bragg) angle  $\theta_B$  of the input light beam, given by

$$\sin \theta_B = \frac{K}{2k} = \frac{\lambda}{2\Lambda n_{\text{eff}}}. \quad (1)$$

The optical wavenumber  $k = 2\pi n_{\text{eff}}/\lambda$ ,  $n_{\text{eff}}$  is the optical mode index, and  $\lambda$  is the optical wavelength in vacuum. The acoustic wavenumber  $K = 2\pi/\Lambda$ , where  $\Lambda$  is the acoustic wavelength in the LN thin film. For the demonstrated 3-GHz AOFS in this work, we use  $\Lambda = 1.2 \mu\text{m}$ ,  $\lambda = 1.5 \mu\text{m}$ , and  $n_{\text{eff}} = 2.0$  yielding  $\sin \theta_B = 0.3$  ( $\theta_B \sim 18$  degrees). The maximum shifting frequency of  $\sim 9$  GHz for  $\lambda = 1.5 \mu\text{m}$  on the LN thin film occurs when the shifted light is fully reflected by the acoustic grating (in this case,  $\theta_B = \pi/2$  or  $\sin \theta_B = 1$ ).

For our device, the light is coupled onto the chip by a lensed fiber and guided by a rib optical waveguide (top width of 3.5  $\mu\text{m}$ ) that is defined by two grooves on the LN thin film. The grooves are patterned by electron beam lithography using PMMA resist and etched about 550 nm in depth by reactive ion etching using argon gas. Following the waveguide, the input light bends and adiabatically broadens towards the central acousto-optic region at the Bragg angle (Fig. 1(b)). The rib waveguides terminate near the acousto-optic region, and the input light beam then propagates as a two-dimensional Gaussian beam in the LN thin film. The end width of the input waveguides is 18  $\mu\text{m}$  such that the Rayleigh range of the light beam is much larger than the acoustic wave width of 100  $\mu\text{m}$ . A waveguide collects the expanded light beam deflected by the acoustic waves, then tapers to a on-chip routing waveguide. The 40- $\mu\text{m}$  width of the collecting waveguide is experimentally selected to provide the highest collection efficiency. With two optical input waveguides and two output waveguides, our device is configured for either anti-Stokes frequency shifts of the input light at Port A or Stokes frequency shifts of the input light at Port B (Fig. 1(b)).

The thin-film acoustic wave propagates along the  $y$  direction and is electrically generated by an interdigital transducer (IDT) via piezoelectricity. The IDT consists of cross-finger electrodes that are made of a 140-nm-thick aluminum layer deposited by thermal evaporation and patterned by the lift-off process (Fig. 1(c)). The pitch of the IDT electrodes is 580 nm, which is equal to the half acoustic wavelength (in the IDT region). To avoid any acoustic reflection by the chip edge or other devices, etching grooves are fabricated at the far ends to deflect acoustic waves. Otherwise, standing acoustic waves formed by any reflection would result in undesired carrier and sideband light at the output.

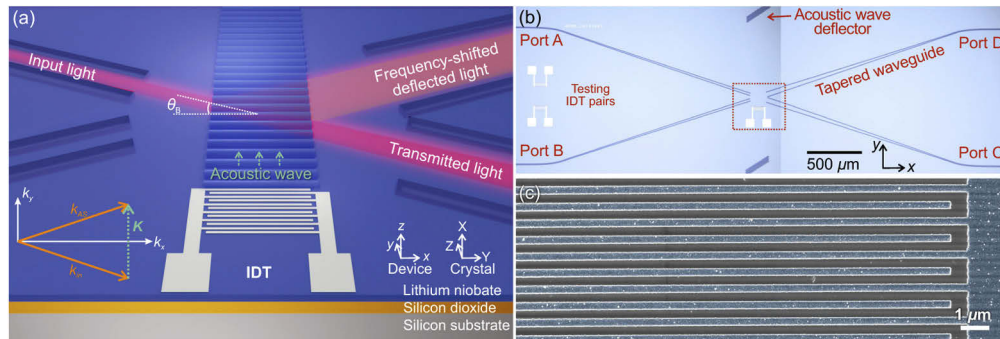


**Fig. 1.** Thin-film lithium niobate (LN) acousto-optic frequency shifter (AOFS). (a) Schematic of the AOFS. The device is on a LN thin film on a silicon dioxide layer. Input light interacts with the traveling acoustic wave generated by the interdigital transducer (IDT), is partially deflected by the Bragg angle, and is frequency shifted by the acoustic frequency. The LN thin film is X cut, the coordinates for the crystal and device are shown. The input light, the deflected light, and the acoustic wave satisfy energy and momentum matching conditions (Inset). (b) Microscopic image of the fabricated device. Optical waveguides are coupled using lensed fibers and broaden to the acousto-optic region, as indicated by the red dashed lines. A pair of IDTs featuring the same specifications are added for characterizing the microwave-to-acoustic transduction. This image is stitched from two microscopic fields of view. (c) False-colored scanning electron microscopic image of the IDT. The aluminum region is in blue.

### 3. Acousto-optic interactions

To characterize the microwave-to-acoustic transduction by the IDT, we measure the microwave reflection and transmission scattering ( $S$ ) parameter spectra of an IDT pair (Fig. 2(a)). Multiple acoustic modes are observed in the transmission spectra (labeled I-IV in Fig. 2(a)), consistent with the acoustic modes found in the numerical simulations (Fig. 2(b)). They are referred to as the Rayleigh wave (Mode I), Love wave (Mode II) of LN thin film, and higher-order Love waves (Modes III and IV) that partially propagate in the silicon dioxide underlying layer. We employ the Rayleigh wave (Mode I) for our AOFS due to its highest transduction efficiency. Twenty-five pairs of 100- $\mu\text{m}$ -width electrodes are used in each IDT to match the external impedance of 50  $\Omega$ , as indicated by the over 10 dB dip in the  $S_{11}$  spectrum (Fig. 2(a)). In the case of the highest transmission of  $S_{21} = -10$  dB at 2.9 GHz, assuming the propagation loss and the acoustic reflection by IDTs are small, we can infer a -5 dB (31%) microwave-to-acoustic transduction efficiency for a single IDT. The efficiency is mainly limited by the symmetric IDT design (maximum 50% in one propagating direction) as well as by the mass loading and ohmic loss of aluminum. The fast variations of the  $S_{21}$  spectrum is due to weak acoustic reflections between the IDT test pair.

The optical refractive index variations due to the acoustic wave (Fig. 2(c)) are calculated from a simulated strain profile and the photoelastic coefficients of LN [33]. The refractive index variation in the  $z$  direction ( $\Delta n_z$ ) is slightly larger than that in other directions, and thus the optical TM mode is deflected more efficiently than the TE mode. We perform a three-dimensional finite-difference time-domain (FDTD) method simulation to investigate the spatial mode profile of the light that is deflected by the acoustic grating (see Appendix A for detail). The FDTD simulation features actual device dimensions. Instead of a traveling acoustic wave, the acoustic grating in the FDTD simulation is represented by a steady refractive index profile. This approximation significantly reduces the computational expense without affecting the spatial mode profile of light. Absent the acoustic wave, the input light beam continues propagation, and no deflection is observed (Fig. 2(d)). With the acoustic wave, the input light beam is partially deflected (Fig. 2(e)). The

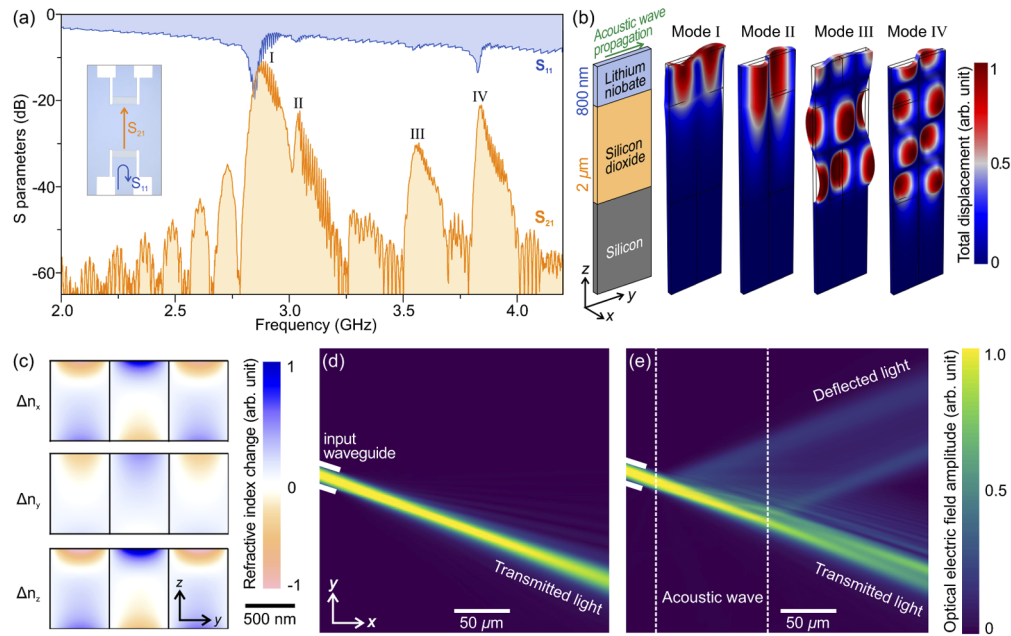


**Fig. 2.** Measurements of microwave-to-acoustic transduction and simulations of acousto-optic interactions. (a) Measured reflection  $S_{11}$  and transmission  $S_{21}$  spectra of an IDT pair. Four acoustic modes (I-IV) are identified in the transmission  $S_{21}$  spectrum. (b) Simulated displacement profiles of acoustic modes corresponding to the peaks in the transmission  $S_{21}$  spectrum. (c) Calculated refractive index variations of the LN thin film induced by the strain fields of acoustic Mode I. The refractive index variations in all directions are normalized using the same scale. (d)(e) Optical electric field profiles from 3D FDTD simulations of the device (d) without and (e) with the acoustic wave. These profiles show the magnitude of optical electric fields at the center of the LN thin film, which is 400 nm from the top surface. All coordinates used here are the device coordinate.

deflected and the transmitted light beams are twice the Bragg angle apart in the far field. The width of the deflected beam is approximately given by

$$w_d \sim 2W \sin \theta_B + w_{in}, \quad (2)$$

where  $W$  is the width of the acoustic grating. For our device, with acoustic width of  $W = 100 \mu\text{m}$  and  $\sin \theta_B = 0.3$ , the width of the deflected beam is  $60 \mu\text{m}$  larger than that of the input beam.

#### 4. Experimental characterization of the LN AOFS

We experimentally characterize our LN AOFS in both the Stokes (Figs. 3(a) and 3(b)) and anti-Stokes (Figs. 3(c) and 3(d)) configurations. We measure the optical spectra of the deflected output light by heterodyne detection using a second laser, which is red-detuned by a few gigahertz from the input laser. The experimental setup is discussed in Appendix B. The wavelength of the input light is 1597 nm, and the IDT is driven at 2.89 GHz with a microwave power of 15 dBm. For the Stokes configuration, the deflected light is red-shifted by 2.89 GHz and exhibits a 31-dB carrier suppression (Fig. 3(b)). The carrier suppression of the deflected light is defined by the ratio of the optical powers at the shifted and carrier frequencies. For the anti-Stokes configuration, the deflected light is blue-shifted, and a 33-dB carrier suppression is observed (Fig. 3(d)). The presence of the carrier frequency light at the deflection output port is most likely caused by the optical scattering due to the on-chip structures, as it exists in absence of the

acoustic wave. The on-to-off extinction ratio at the deflection port is also measured over to be 30 dB. Any other undesired optical sideband is not observed above the noise floor in the heterodyne measurements, thus the sideband suppression rate exceeds 40 dB.

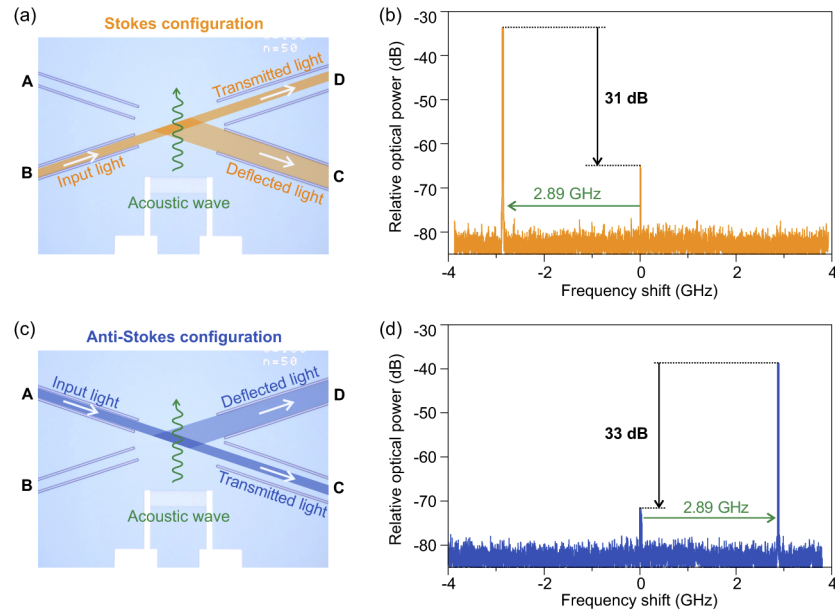


**Fig. 3.** Measurements of the acousto-optic frequency shifting. (a) Configuration for Stokes frequency shifting and (b) heterodyne measurement of frequency shifted light at Port C. (c) Configuration for anti-Stokes frequency shifting and (d) heterodyne measurement of frequency shifted light at Port D.

We further characterize the efficiencies and bandwidths of our AOFS in the anti-Stokes configuration (Fig. 4). An insertion loss of -15 dB is determined by fiber-to-fiber optical transmission measurements through the transmitted light port. This loss is mainly due to the optical mode mismatch between the single-mode lensed fibers and waveguides and could be reduced by employing an on-chip coupler [34]. We define the on-chip frequency shifting efficiency as the ratio of optical powers between the deflected light and the transmitted light (when microwave input is off) collected by the single-mode lensed fiber. We use a fiber polarization controller at the input fiber to maximize the deflection efficiency. The measured efficiency linearly raises with microwave power and reaches 3.5% with a 30-dBm microwave power applied to the IDT pads (Fig. 4(a)). Further increase of the microwave power can damage the IDT electrodes.

The optical bandwidth can be estimated as  $\frac{\Delta}{w} \lambda$  [35], which in our case gives a theoretically predicted bandwidth of 19 nm. The measured optical bandwidth of our AOFS is 14 nm, which is close to predicted value (Fig. 4(b)). The discrepancy could be attributed to the mode couplings in the wide waveguides.

We measured the frequency-shifted optical power with varied microwave frequency (Fig. 4(c)). We perform the homodyne detection of the deflected light. The 3-dB microwave bandwidth of our AOFS is 70 MHz for the Rayleigh mode (Mode I in Fig. 4(c)), which is determined by the IDT design. Although other acoustic modes have different frequencies, they feature a similar acoustic wavelength as defined by the IDT electrode pitch, and thus deflect the light at the same Bragg angle.

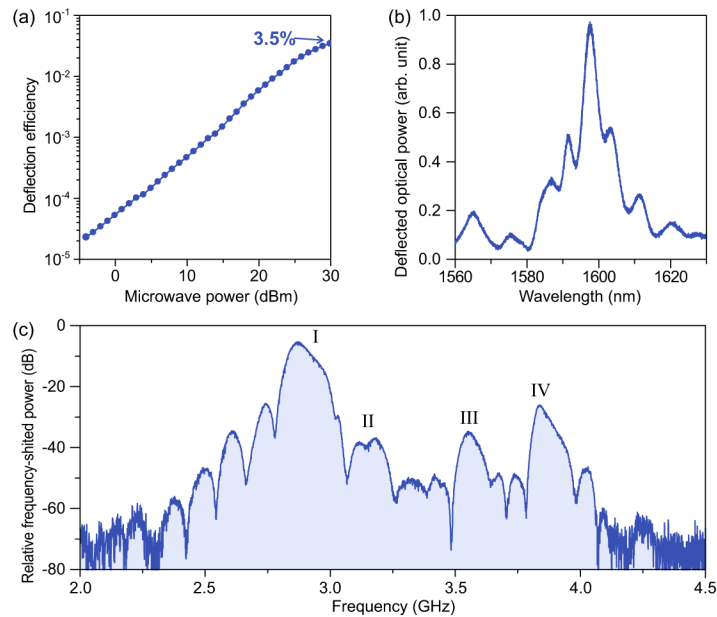


**Fig. 4.** Characterization of the LN AOFS. (a) Efficiency of the AOFS for varying microwave driving power. (b) Deflected optical power for different wavelengths of the input light. For measurements in (a) and (b), the acoustic frequency is 2.89 GHz. (c) Relative optical power of the frequency-shifted light for varying microwave frequency using the homodyne detection. For measurements in (a) and (c), the input optical wavelength is 1597 nm. Data in Figs. 3 and 4 are measured from the same device.

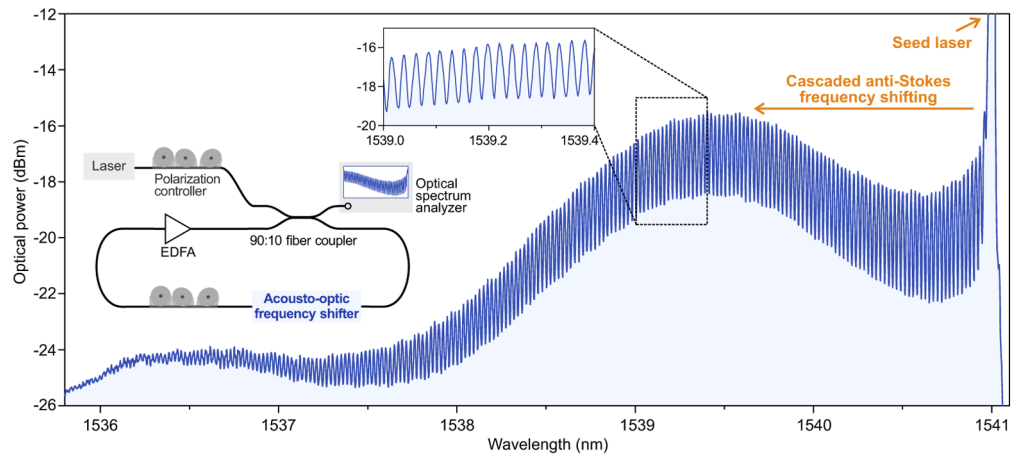


**Fig. 5.** Optical frequency comb generation using an active frequency shifting loop. The wavelength of the seed laser is 1541 nm. Inset: schematic of the setup for acousto-optic comb generation and magnification of the optical spectrum. The optical spectrum analyzer features a resolution bandwidth of 0.02 nm (2.5 GHz at 1540 nm).

## 5. Acousto-optic frequency comb generation

An active acousto-optic frequency shifting loop, also known as frequency-shifted feedback laser [36] can be used for optical frequency combs and pulse generation [37–39]. Moreover, this approach is of interest for various applications in optical real-time Fourier transformations [40], photonic microwave channeling [41], and optical frequency domain ranging [42]. For these applications, a broad frequency comb with gigahertz frequency spaced lines could improve bandwidth or ranging resolution. Here, we generate an optical frequency comb with a 2.9 GHz line spacing using an active acousto-optic frequency shifting loop (Fig. 5). The loop contains our AOFS and an erbium-doped fiber amplifier (EDFA) to compensate the optical loss (Fig. 5 Inset). The loop is seeded with a laser at 1541 nm and couples light in and out by a 2×2 90:10 fiber coupler. The Bragg angle of the AOFS is chosen to be 17.45 degree to match the operating optical wavelength of our EDFA. The generated frequency comb features over 200 comb lines spanning 0.6 THz (5 nm) optical bandwidth.

The comb bandwidth is mainly limited by the gain saturation of the EDFA, in which the gain is reduced after the light has taken hundreds of round trips. The demonstrated gigahertz acousto-optic frequency comb could find applications in dual-comb spectroscopy [43], wavelength-division-multiplexed communication, and on-chip short-pulse generation.

## 6. Discussion and outlook

We demonstrate an integrated gigahertz AOFS on a thin-film-LN-on-oxide substrate. We can design devices with shift frequencies from hundreds of MHz to a few GHz by adjusting the Bragg angle. Higher shift frequencies are possible for shorter optical wavelengths [44] or using materials with higher acoustic speed, such as aluminum nitride. The microwave bandwidth could be extended by using multiple IDTs or chirped IDTs [45]. The optical wavelength of our AOFSs can be designed to any wavelength in the transparency window of LN, which is from visible to mid-infrared. For mid-infrared AOFSs, LN on sapphire substrates could be utilized to avoid optical absorption by the underlying oxide layer. Although the efficiency of our AOFS is currently only 3.5%, it could be further improved by employing unidirectional IDTs [46] that could yield a 3 dB higher microwave-to-acoustic transduction efficiency than symmetric IDTs. Acoustic resonators [47] could be employed to reduce the input microwave power for acousto-optic intensity modulators, in which the input light could be deflected by a resonant standing acoustic mode. A wider acoustic wave could also improve the deflection efficiency at the same total acoustic power [4]. However, as discussed in Eq. (2), widening the acoustic wave also broadens the deflected beam, which could be challenging for collecting the light back to a single mode waveguide, especially for large Bragg angles  $\theta_B$  (high shift frequencies). An on-chip lens [48] may be employed to better collect the broadened deflected light into a waveguide. Moreover, our integrated acousto-optic platform, in which light is deflected by acoustic waves, would lead to the development of on-chip optical routers, isolators, and scanners [35], microwave spectral analyzers [49], and carrier-envelope phase stabilizer [50].

## Appendix A: FDTD simulation

To investigate the Bragg diffraction by the acoustic mode (grating), we perform a three-dimensional (3D) finite-difference time-domain (FDTD) method simulation using *Lumerical FDTD Solutions*. We simulate the acousto-optic interaction of our device using its actual dimensions. The configuration of the simulation is illustrated in Fig. 6. The acoustic grating is simulated by a 3D refractive index profile. Since the shifting frequency ( $\sim 3$  GHz) is small compared to the optical frequency ( $\sim 200$  THz), the optical modes are approximately same at unshifted and shifted optical frequencies. The steady refractive index profile is thus used to significantly reduce the computational expense without affecting the spatial profiles. The input waveguide is formed by

two etched grooves and is excited by the fundamental TM mode. The outer boundaries of the simulation region are set to the perfectly matched layers for the optical light. The optical profile monitor at  $0.4 \mu\text{m}$  from the top surface of the  $0.8 \mu\text{m}$  lithium niobate layer is shown in Figs. 2(d) and 2(e).

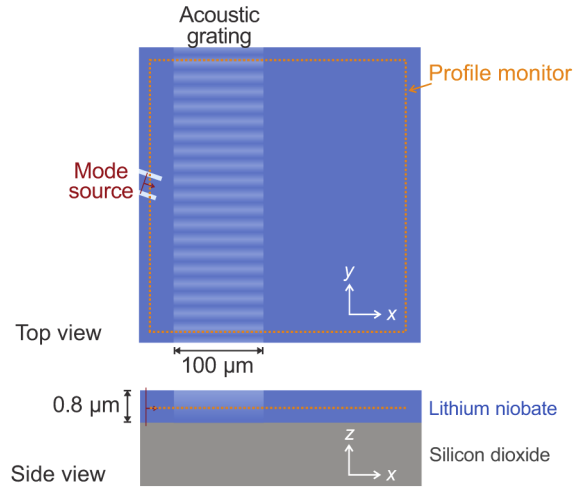


**Fig. 6.** Configuration of the FDTD simulation. The  $0.8 \mu\text{m}$  lithium niobate layer is on silicon dioxide. The acoustic grating is simulated by a refractive index profile, which is derived from the strain profile of the acoustic wave. The input waveguide is excited by a fundamental TM mode.

The simulated far-field pattern after the acoustic grating (Fig. 7) shows the transmitted light at the input Bragg angle ( $\sin \theta = -0.3$ ) of the acoustic grating and the deflected light at the opposite Bragg angle ( $\sin \theta = 0.3$ ).

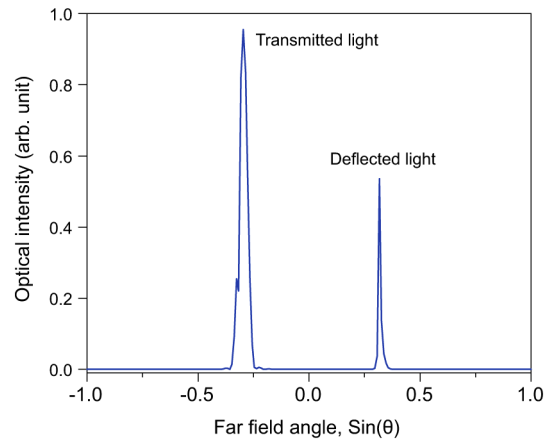


**Fig. 7.** Simulated far-field pattern of the light after the acoustic grating. The deflected light propagates at the Bragg angle of  $\sin \theta_B = 0.3$ .

## Appendix B: Experimental setups

The schematic diagrams of the heterodyne and the homodyne detection setups are shown in Figs. 8 and 9, respectively.



The heterodyne measurement uses two lasers and the Stokes and anti-Stokes frequency shifts are distinguished relative to the input carrier light. Here, the reference Laser 2 is red detuned from the input Laser 1.

The homodyne measurement uses the light from the same input laser in detection. This avoids frequency drifting between two lasers and reduces the noise floor on the spectrum analyzer by using narrow bandwidth, which increases the detection time.

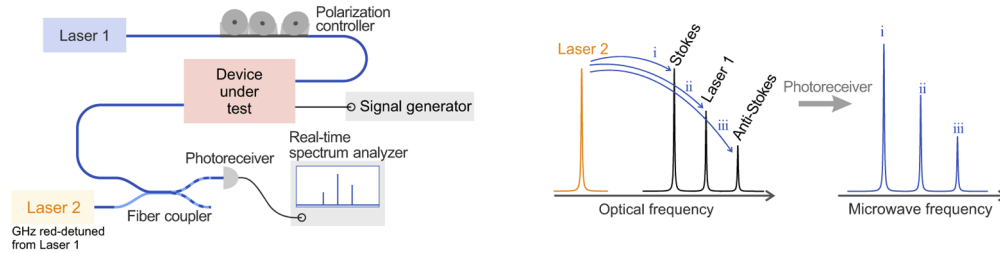


**Fig. 8.** The schematic diagrams of the heterodyne detection. The deflected output light from the device beats with a red-detuned Laser 2 on the photoreceiver and generates microwave signals corresponding to the carrier, the Stoke, and the anti-Stokes light.

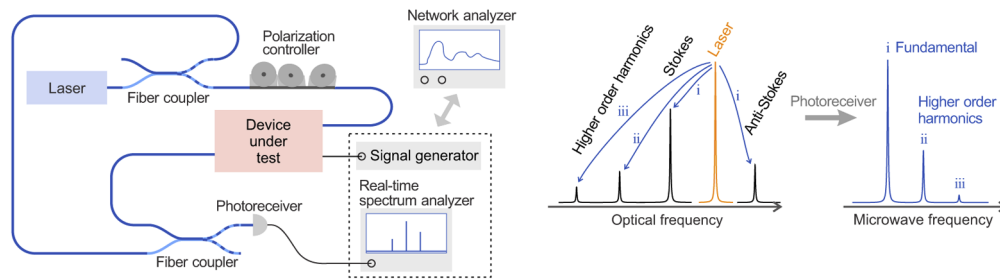


**Fig. 9.** The schematic diagrams of the homodyne detection. The deflected output light from the device beats with the input laser on the photoreceiver and generates microwave signals corresponding fundamental and higher order harmonic lights of the AOFS. The signal generator and the real-time spectrum analyzer are used for characterizing nonlinearity, and the network analyzer is used for characterizing the microwave bandwidth of the device.

## Funding

Alliance for Quantum Technologies; U.S. Department of Energy (DE-SC0019219); Natural Sciences and Engineering Research Council of Canada; Raytheon Company (A40210); Office of Naval Research (N00014-15-1-2761); National Science Foundation (1541959, DMR-1231319, IIP-1827720).

## Acknowledgments

We thank Mo Li and Huan Li for fruitful discussions. This work was performed in part at the Center for Nanoscale Systems (CNS), a member of the National Nanotechnology Coordinated Infrastructure Network (NNCI). CNS is part of Harvard University.

## Disclosures

M.L.: HyperLight Corporation (I, C); Raytheon (F). This document does not contain technology or Technical Data controlled under either the U.S. International Traffic in Arms Regulations or the U.S. Export Administration Regulations.

## References

1. B. J. Eggleton, C. G. Poulton, P. T. Rakich, M. J. Steel, and G. Bahl, "Brillouin integrated photonics," *Nat. Photonics* **13**(10), 664–677 (2019).
2. Z. Y. Cheng and C. S. Tsai, "Baseband integrated acousto-optic frequency shifter," *Appl. Phys. Lett.* **60**(1), 12–14 (1992).
3. C. Dong, V. Fiore, M. C. Kuzyk, L. Tian, and H. Wang, "Optical wavelength conversion via optomechanical coupling in a silica resonator," *Ann. Phys.* **527**(1-2), 100–106 (2015).
4. H. Li, Q. Liu, and M. Li, "Electromechanical Brillouin scattering in integrated planar photonics," *APL Photonics* **4**(8), 080802 (2019).
5. Q. Liu, H. Li, and M. Li, "Electromechanical Brillouin scattering in integrated optomechanical waveguides," *Optica* **6**(6), 778–785 (2019).
6. K. C. Balram, M. I. Davanco, J. D. Song, and K. Srinivasan, "Coherent coupling between radio frequency, optical, and acoustic waves in piezo-optomechanical circuits," *Nat. Photonics* **10**(5), 346–352 (2016).
7. L. Cai, A. Mahmoud, M. Khan, M. Mahmoud, T. Mukherjee, J. Bain, and G. Piazza, "Acousto-optical modulation of thin film lithium niobate waveguide devices," *Photonics Res.* **7**(9), 1003–1013 (2019).
8. W. Jiang, R. N. Patel, F. M. Mayor, T. P. McKenna, P. Arrangoiz-Arriola, C. J. Sarabalis, J. D. Witmer, R. Van Laer, and A. H. Safavi-Naeini, "Lithium niobate piezo-optomechanical crystals," *Optica* **6**(7), 845–853 (2019).
9. W. Jiang, C. J. Sarabalis, Y. D. Dahmani, R. N. Patel, F. M. Mayor, T. P. McKenna, R. Van Laer, and A. H. Safavi-Naeini, "Efficient bidirectional piezo-optomechanical transduction between microwave and optical frequency," *Nat. Commun.* **11**(1), 1166 (2020).
10. H. Liang, R. Luo, Y. He, H. Jiang, and Q. Lin, "High-quality lithium niobate photonic crystal nanocavities," *Optica* **4**(10), 1251 (2017).
11. L. Shao, M. Yu, S. Maity, N. Sinclair, L. Zheng, C. Chia, A. Shams-Ansari, C. Wang, M. Zhang, K. Lai, and M. Lončar, "Microwave-to-optical conversion using lithium niobate thin-film acoustic resonators," *Optica* **6**(12), 1498–1505 (2019).
12. D. Marpaung, B. Morrison, M. Pagani, R. Pant, D.-Y. Choi, B. Luther-Davies, S. J. Madden, and B. J. Eggleton, "Low-power, chip-based stimulated Brillouin scattering microwave photonic filter with ultrahigh selectivity," *Optica* **2**(2), 76–83 (2015).
13. A. A. Savchenkov, A. B. Matsko, V. S. Ilchenko, D. Seidel, and L. Maleki, "Surface acoustic wave opto-mechanical oscillator and frequency comb generator," *Opt. Lett.* **36**(17), 3338–3340 (2011).
14. L. Fan, C.-L. Zou, N. Zhu, and H. X. Tang, "Spectrotemporal shaping of itinerant photons via distributed nanomechanics," *Nat. Photonics* **13**(5), 323–327 (2019).
15. S. Gundavarapu, G. M. Brodnik, M. Puckett, T. Huffman, D. Bose, R. Behunin, J. Wu, T. Qiu, C. Pinho, N. Chauhan, J. Nohava, P. T. Rakich, K. D. Nelson, M. Salit, and D. J. Blumenthal, "Sub-hertz fundamental linewidth photonic integrated Brillouin laser," *Nat. Photonics* **13**(1), 60–67 (2019).
16. N. T. Otterstrom, R. O. Behunin, E. A. Kittlaus, Z. Wang, and P. T. Rakich, "A silicon Brillouin laser," *Science* **360**(6393), 1113–1116 (2018).
17. K. Fang, J. Luo, A. Metelmann, M. H. Matheny, F. Marquardt, A. A. Clerk, and O. Painter, "Generalized non-reciprocity in an optomechanical circuit via synthetic magnetism and reservoir engineering," *Nat. Phys.* **13**(5), 465–471 (2017).
18. J. Kim, M. C. Kuzyk, K. Han, H. Wang, and G. Bahl, "Non-reciprocal Brillouin scattering induced transparency," *Nat. Phys.* **11**(3), 275–280 (2015).
19. E. A. Kittlaus, N. T. Otterstrom, P. Kharel, S. Gertler, and P. T. Rakich, "Non-reciprocal interband Brillouin modulation," *Nat. Photonics* **12**(10), 613–619 (2018).
20. N. T. Otterstrom, E. A. Kittlaus, S. Gertler, R. O. Behunin, A. L. Lentine, and P. T. Rakich, "Resonantly enhanced nonreciprocal silicon Brillouin amplifier," *Optica* **6**(9), 1117–1123 (2019).
21. E. A. Kittlaus, W. M. Jones, P. T. Rakich, N. T. Otterstrom, R. E. Muller, and M. Rais-Zadeh, "Electrically-driven acousto-optics and broadband non-reciprocity in silicon photonics," arXiv e-prints p. 2004.01270 (2020).
22. D. B. Sohn and G. Bahl, "Direction reconfigurable nonreciprocal acousto-optic modulator on chip," *APL Photonics* **4**(12), 126103 (2019).
23. D. B. Sohn, S. Kim, and G. Bahl, "Time-reversal symmetry breaking with acoustic pumping of nanophotonic circuits," *Nat. Photonics* **12**(2), 91–97 (2018).
24. N. Savage, "Acousto-optic devices," *Nat. Photonics* **4**(10), 728–729 (2010).
25. K. Higuma, S. Oikawa, Y. Hashimoto, H. Nagata, and M. Izutsu, "X-cut lithium niobate optical single-sideband modulator," *Electron. Lett.* **37**(8), 515–516 (2001).

26. Y. Ogiso, Y. Tsuchiya, S. Shinada, S. Nakajima, T. Kawanishi, and H. Nakajima, "High extinction-ratio integrated Mach-Zehnder modulator with active y-branch for optical ssb signal generation," *IEEE Photonics Technol. Lett.* **22**(12), 941–943 (2010).
27. R. Houtz, C. Chan, and H. Müller, "Wideband, efficient optical serrodyne frequency shifting with a phase modulator and a nonlinear transmission line," *Opt. Express* **17**(21), 19235–19240 (2009).
28. D. M. S. Johnson, J. M. Hogan, S. w. Chiow, and M. A. Kasevich, "Broadband optical serrodyne frequency shifting," *Opt. Lett.* **35**(5), 745–747 (2010).
29. T. Spuesens, Y. Li, P. Verheyen, G. Lepage, S. Balakrishnan, P. Absil, and R. Baets, "Integrated optical frequency shifter on a silicon platform," in *Conference on Lasers and Electro-Optics*, (Optical Society of America, 2016), OSA Technical Digest (2016), p. SF2G.1.
30. S. F. Preble, Q. Xu, and M. Lipson, "Changing the colour of light in a silicon resonator," *Nat. Photonics* **1**(5), 293–296 (2007).
31. A. A. Savchenkov, W. Liang, A. B. Matsko, V. S. Ilchenko, D. Seidel, and L. Maleki, "Tunable optical single-sideband modulator with complete sideband suppression," *Opt. Lett.* **34**(9), 1300–1302 (2009).
32. B.-M. Yu, J.-M. Lee, C. Mai, S. Lischke, L. Zimmermann, and W.-Y. Choi, "Single-chip Si optical single-sideband modulator," *Photonics Res.* **6**(1), 6–11 (2018).
33. A. S. Andrushchak, B. G. Mytsyk, H. P. Laba, O. V. Yurkevych, I. M. Solskii, A. V. Kityk, and B. Sahraoui, "Complete sets of elastic constants and photoelastic coefficients of pure and MgO-doped lithium niobate crystals at room temperature," *J. Appl. Phys.* **106**(7), 073510 (2009).
34. L. He, M. Zhang, A. Shams-Ansari, R. Zhu, C. Wang, and M. Lončar, "Low-loss fiber-to-chip interface for lithium niobate photonic integrated circuits," *Opt. Lett.* **44**(9), 2314–2317 (2019).
35. B. E. Saleh and M. C. Teich, *Fundamentals of photonics* (John Wiley & Sons, 1991). Chap. 20 Acousto-optics.
36. H. Guillet de Chatellus, E. Lacot, W. Glastre, O. Jacquin, and O. Hugon, "Theory of talbot lasers," *Phys. Rev. A* **88**(3), 033828 (2013).
37. V. Durán, H. G. d. Chatellus, C. Schnébelin, K. Nithyanandan, L. Djevarhidjian, J. Clement, and C. R. Fernández-Pousa, "Optical frequency combs generated by acousto-optic frequency-shifting loops," *IEEE Photonics Technol. Lett.* **31**(23), 1878–1881 (2019).
38. P. D. Hale and F. V. Kowalski, "Output characterization of a frequency shifted feedback laser: theory and experiment," *IEEE J. Quantum Electron.* **26**(10), 1845–1851 (1990).
39. F. V. Kowalski, J. A. Squier, and J. T. Pinckney, "Pulse generation with an acousto-optic frequency shifter in a passive cavity," *Appl. Phys. Lett.* **50**(12), 711–713 (1987).
40. H. Guillet de Chatellus, L. R. Cortés, and J. Azaña, "Optical real-time fourier transformation with kilohertz resolutions," *Optica* **3**(1), 1–8 (2016).
41. W. Hao, Y. Dai, F. Yin, Y. Zhou, J. Li, and K. Xu, "Photonic microwave channelization based on frequency shifted feedback laser and delayed coherent detection," in *Conference on Lasers and Electro-Optics*, (Optical Society of America, 2018), OSA Technical Digest (online), p. JW2A.73.
42. K. Nakamura, T. Hara, M. Yoshida, T. Miyahara, and H. Ito, "Optical frequency domain ranging by a frequency-shifted feedback laser," *IEEE J. Quantum Electron.* **36**(3), 305–316 (2000).
43. V. Durán, C. Schnébelin, and H. Guillet de Chatellus, "Coherent multi-heterodyne spectroscopy using acousto-optic frequency combs," *Opt. Express* **26**(11), 13800–13809 (2018).
44. B. Desiatov, A. Shams-Ansari, M. Zhang, C. Wang, and M. Lončar, "Ultra-low-loss integrated visible photonics using thin-film lithium niobate," *Optica* **6**(3), 380–384 (2019).
45. D. Fall, M. Duquenooy, M. Ouaftouh, N. Smagin, B. Piwakowski, and F. Jenot, "Generation of broadband surface acoustic waves using a dual temporal-spatial chirp method," *J. Acoust. Soc. Am.* **142**(1), EL108–EL112 (2017).
46. S. Lehtonen, V. P. Plessky, C. S. Hartmann, and M. M. Salomaa, "Unidirectional SAW transducer for gigahertz frequencies," *IEEE Trans. Ultrason., Ferroelect., Freq. Contr.* **50**(11), 1404–1406 (2003).
47. L. Shao, S. Maity, L. Zheng, L. Wu, A. Shams-Ansari, Y.-I. Sohn, E. Puma, M. N. Gadalla, M. Zhang, C. Wang, E. Hu, K. Lai, and M. Lončar, "Phononic band structure engineering for high-Q gigahertz surface acoustic wave resonators on lithium niobate," *Phys. Rev. Appl.* **12**(1), 014022 (2019).
48. G. Ren, T. G. Nguyen, and A. Mitchell, "Gaussian beams on a silicon-on-insulator chip using integrated optical lenses," *IEEE Photonics Technol. Lett.* **26**(14), 1438–1441 (2014).
49. T. M. Turpin, "Spectrum analysis using optical processing," *Proc. IEEE* **69**(1), 79–92 (1981).
50. S. Koke, C. Grebing, H. Frei, A. Anderson, A. Assion, and G. Steinmeyer, "Direct frequency comb synthesis with arbitrary offset and shot-noise-limited phase noise," *Nat. Photonics* **4**(7), 462–465 (2010).